

# Large Rashba Spin-Orbit Effect by Orbital Engineering at SrTiO<sub>3</sub>-based Correlated Interfaces

G. J. Omar<sup>1,†</sup>, W. L. Kong<sup>1,†</sup>, H. Jani<sup>1</sup>, M. S. Li<sup>2</sup>, J. Zhou<sup>1</sup>, Z. S. Lim<sup>1</sup>, S. Prakash<sup>1</sup>, S. W. Zeng<sup>1</sup>, S. Hooda<sup>3</sup>, T. Venkatesan<sup>3</sup>, Y. P. Feng<sup>1</sup>, S. J. Pennycook<sup>2</sup>, L. Shen<sup>4</sup>, A. Ariando<sup>1,\*</sup>

## Affiliations:

<sup>1</sup>Department of Physics, Faculty of Science, National University of Singapore, Singapore 117542, Singapore

<sup>2</sup>Department of Materials Science and Engineering, National University of Singapore, Singapore 117575, Singapore

<sup>3</sup>Department of Electrical and Computer Engineering, National University of Singapore, Singapore 117576, Singapore

<sup>4</sup>Department of Mechanical Engineering, National University of Singapore, Singapore, 117575

\*Correspondence should be sent to [ariando@nus.edu.sg](mailto:ariando@nus.edu.sg)

† Authors contributed equally.

## Abstract

**Large spin-orbit effect is an essential element for efficient spin-orbitronics that utilizes the interplay between charge and spin degree of freedom. This spin-orbit effect is generally small in heavy-metal<sup>1-7</sup>-based or requires large external applied voltages in complex-oxide-based heterostructures<sup>8</sup>. Here, we present a large Rashba spin orbit effect at zero applied voltages by interfacial atomic control of orbital hybridization that introduces Ti-O lattice polarization at the SrTiO<sub>3</sub>-based interfaces. The observed spin orbit effect ( $\sim 3.5 \times 10^{-12}$  eV-m) is four-fold larger than that observed in conventional SrTiO<sub>3</sub>-based interfaces at zero bias voltage. The orbital hybridization and Ti-O lattice polarization are verified through *ab initio* electronic structure calculations and high-resolution atomic microscopy. Our results present a unique approach to achieve Ti-O lattice polarization at SrTiO<sub>3</sub> interfaces and open hitherto unexplored avenues of generating and controlling Rashba spin orbit effect via orbital engineering to design next-generation spin-orbitronics.**

In condensed matter physics, spin-orbit coupling (SOC) is intrinsic property of material and links to the quantum particle's spin  $\sigma$  and momentum  $\mathbf{k}$ . This SOC effect and its tunability have been proposed to be a potential route for developing function devices utilizing spin degrees of freedom, which reduces the energy efficiency of spintronic devices<sup>9,10</sup>. This SOC effect regulates the spin population decay and thus defines its suitability in new device architecture, namely spin-orbitronics<sup>11</sup>. Of particular interest is the Rashba SOC<sup>12</sup>, which is a relativistic effect associated with an inversion symmetry breaking typically found in a two-dimensional or an interfacial system. This effect lifts the spin degeneracy states at  $k$ -points in the Brillouin zone due to a symmetry-breaking electric field ( $E_0$ ) normal to the interface. In Rashba SOC, the Hamiltonian is defined by  $H_R = \alpha_R \hat{\mathbf{z}} \cdot (\mathbf{k} \times \boldsymbol{\sigma})$ , where  $\alpha_R$  is the Rashba SOC coefficient and  $\hat{\mathbf{z}}$  is the Rashba unit vector normal to the interface. It is responsible for the emergent phenomena in various condensed matter systems such as graphene, topological insulators, and cold atoms<sup>13,14</sup>.

The canonical model of the two-dimensional electron system (2DES) at the interface between LaAlO<sub>3</sub> (LAO) and insulators SrTiO<sub>3</sub> (STO) have been shown to exhibit a strong Rashba SOC with long carrier lifetimes (crucial for low power spintronics<sup>15-18</sup>). It is well accepted that the polar nature of the LAO crystal can lead to a diverging internal potential and electronic reconstruction when the LAO is deposited onto a nonpolar STO. The electronic reconstruction results in a charge transfer from the LAO into STO and thus forms 2DES at the LAO/STO complex oxide heterostructures. Rashba strength can be read off the band structure by identifying the orbital hybridization of interfacial systems. This orbital hybridization is strongly sensitive to local orbital and lattice polarization of STO interface<sup>19</sup>. Here, the hybridization of  $t_{2g}$  electron of Ti atoms at STO interface plays an important role and the Hamiltonian  $H$  is defined as  $H = H_0 + H_{ASO} + H_z$ . Here,  $H_0$  is the intra-orbital hopping (diagonal in the orbital space),  $H_{ASO}$  is the on-site atomic SOC, and  $H_z$  is the antisymmetric inter-orbital hopping<sup>19-22</sup>. These various intra- and inter-orbital perturbed hopping terms between the energy bands influence the energy dispersion and SOC. In particular, the  $H_z$  term generates electronic hopping from  $d_{xy}$  to  $d_{zx}$  along the  $y$  direction via  $p_x$  and from  $d_{xy}$  to  $d_{yz}$  along the  $x$  direction via  $p_y$  in the second-order perturbation producing a Rashba-like SOC effect at the STO interface.

The building up of the electric field perpendicular to the STO interface produces opposite forces on the Ti cations and oxygen anions (**Figure 1**). The polarization in the TiO<sub>2</sub> plane induces Ti-O-Ti bond angle resulting in a layer dependent ionic displacement. The ionic displacement is related to the asymmetric features and hybridization of the interface wave functions, which controls the strength of the Rashba SOC. In the electron crystal momentum  $\mathbf{k} = (k_x, k_y, 0)$ , Pauli matrices  $\boldsymbol{\sigma} = (\sigma_x, \sigma_y, \sigma_z)$ , and orbital basis  $(yz, zx, xy)$ , the antisymmetric hopping Hamiltonian term  $H_z$  takes the form,

$$H_z = \Delta_z \begin{pmatrix} 0 & 0 & ik_x \\ 0 & 0 & ik_y \\ -ik_x & -ik_y & 0 \end{pmatrix} \otimes \sigma^0 \begin{Bmatrix} yz \\ zx \\ xy \end{Bmatrix}, \quad (1)$$

where  $\Delta_z = \gamma_1 t_{pd} E_0 / \Delta_{pd} + (n t_{pd}^2 / \Delta_{pd})$  is related to the induced orbital polarization arising from the additional electric field (with hopping amplitude  $E_0 \gamma_1$ ) and bond angle,  $n$ , or ionic polarization/

displacement ( $\Delta\delta_{\text{Ti-O}}$ ) along the  $z$  direction, mediated by the  $p$ - $d$  hybridized orbitals with the hopping amplitude  $t_{pd}$ . Here  $\Delta_{pd}$  is the splitting between the O- and Ti-orbitals. The  $\Delta_z$  is a layer-dependent parameter, having a maximum value at the interface and decreasing rapidly at the deeper layers. This hybridization within the  $t_{2g}$  manifold, in the orbital network  $\text{Ti}(3d_{zx}) - \text{O}(2p_x) - \text{Ti}(3d_{xy})$ , directly contributes to  $H_{SO}$  and consequently leads to a Rashba splitting. A brief description of all the Hamiltonians is described in **Supplementary information S1**. **Figure 1(a)** illustrate the lattice displacement of the  $\text{Ti}(3d_{zx}) - \text{O}(2p_x) - \text{Ti}(3d_{xy})$  orbitals of the  $\text{TiO}_2$  layer. Larger the orbital displacement induces more built-in electric field, results in enhancing the Rashba SOC.

This present work focuses on providing experimental evidence of controlling Rashba SOC (at zero bias) in LAO/STO interfaces from the theory of  $t_{2g}$  Rashba interfaces via antisymmetric orbital hybridization. To examine the pronounced contribution of the antisymmetric hopping, LAO and STO interface is modulated with a  $\text{LaFeO}_3$  (LFO) buffer layer with thickness of  $d = 0$  to 6-unit cells (uc). We demonstrate a fourfold enhancement of the Rashba SOC that can be modulated with LFO engineering layer. We, therefore, fabricated LAO and STO complex oxide heterostructures with LFO buffer layer via pulsed laser deposition (PLD) system. A reflection high-energy electron diffraction (RHEED) method was used to confirm the layer-by-layer growth during the deposition (see **Supplementary Information**). The atomic structure of the interfaces was characterized using a cross-sectional high-angle annular dark-field (HAADF) mode of the scanning tunnelling electron microscopy (STEM). STEM images consistently present a coherent and epitaxial growth with atomically sharp interfaces with  $d = 0, 2$ , and 4 uc (schematic **Figure 1(b)** and **Supplementary Information S4**).

As stated, the ionic displacement is associated with an internal electric field  $E_0$  and is directly responsible for the Rashba interaction parameters. We, therefore, calculated the increase in the distortion of the  $\text{TiO}_2$  plane in LAO/STO interfaces with and without LFO layer using *ab-initio* calculation theoretically. First-principles calculations with Vienna *ab-initio* simulations package (VASP) are used to study the effects of the LFO layer to the interfacial Rashba SOC. A schematic diagram of the LAO/LFO/STO interface showing a Ti-O-Ti ionic displacement ( $\Delta\delta_{\text{Ti-O}}$ ) along the

[001] axis for the topmost TiO<sub>2</sub> plane is shown in **Figure 1(c)** and zoom in **Figure 1(d)**. The ionic displacements derived from the first-principles calculations ( $\Delta\delta_{\text{Ti-O}}$ ) of the TiO<sub>2</sub> layer at different depths from the interface for  $d = 0$  and 4 uc are given in **Figure 1(e)**. The lattice distortion is calculated from the displacement of the ions along the [001] axis relative to the center of the Ti- and O-sites. We can see that for the heterostructure with a LFO layer, the first STO layer near the interface has a pronounced ionic displacement ( $\Delta\delta_{\text{Ti-O}}$ ) compared to that without the LFO layer. We verify this lattice displacement experimentally using annular bright-field (ABF) mode in the STEM for the  $d = 4$  uc sample (**Figure 1(f)**). Lattice displacement values are averaged over each layer, and the error bars represent the standard deviations of O-anions (Ti-cations) corresponds to the upwards (downwards) displacement configuration, which is plotted as solid circles in **Figure 1(g)**. It shows a displacement of the Ti atom of around 0.016 nm in the topmost STO layer (purple solid circles), which is larger than that without the LFO layer (in orange diamond)<sup>23</sup>. This implies that the effective electric field at the interface is higher after the incorporation of the modulation layer, resulting in the pronounced enhancement of the Rashba SOC. Our results can finally be explained using an asymmetric orbital hybridization of the interface wave functions which influences the orbital and lattice polarization of the STO layer.

Furthermore, we discuss the transport characteristics where **Figure 2(a)** shows the sheet resistance ( $R_{xx}$ ) as a function of temperature between 3-300 K for various LAO/STO heterostructure. Increasing  $d$  leads to a suppression of the charge transfer and the 2DES carrier density, resulting in enhancement of the longitudinal resistivity. Eventually, a metal-to-insulator transition is observed at  $d = 6$  uc (yellow shaded area in Fig. 2(a)), as we have reported earlier<sup>24</sup>. As the LFO layer is also polar, the relatively smaller internal electric field of the LFO per unit cell, however, would require  $\sim 50$  uc of LFO to have enough electric field to induce a charge transfer<sup>16,25</sup>. Hence, all our LFO/STO interfaces are indeed always insulating<sup>24</sup>. **Figure 2(b)** shows the sheet carrier densities ( $n_S$ ) of our LAO/LFO/STO heterostructures, which are typically lower than the universal carrier density ( $1.68 \pm 0.18 \times 10^{13} \text{ cm}^{-2}$ ) of the 2DES at the LAO/STO interface<sup>26</sup>. The low carrier density indicates that only one of the Ti 3d orbitals is being occupied, that is the lowest Ti  $d_{xy}$  band. The linear Hall resistance

up to 9 T further supports this single-band occupancy and is similar to that of the LAO/STO below the Lifshitz transition<sup>27</sup>. The electron diffusion constant, calculated as  $D = \frac{1}{2}v_F^2\tau_e$  for this singly occupied  $d_{xy}$  orbital, where Fermi velocity  $v_F = \hbar k_F/m^*$ , Fermi momentum  $k_F = \sqrt{2\pi n_S}$ , and  $m^*$  is the effective mass, decreases with increasing  $d$  (**Figure 2(c)**).

Experimentally, Rashba SOC was typically calculated from low-temperature magnetotransport using a quantum correction associated with the weak antilocalization (WAL)<sup>28,29</sup> and tuning of the Rashba SOC has also been demonstrated using electrostatic fields<sup>8,30-34</sup>. Although inversion symmetry is naturally broken at STO interfaces, maximizing the influence of this effect at zero bias voltage on the electronic states of interest remains elusive. Hence, the enhancement and control of Rashba SOC without external bias are one of the central challenges in the potential utilization of spin-orbitronics for future in-logic memory devices<sup>35</sup>. We, therefore, measured magnetoresistance (MR) measurements on our 2DES samples using a dc four-probe technique in a Hall bar configuration (see **Supplementary Information**). The observed MR is typically positive and increases quadratically in high fields. As the temperature is decreased below 6 K, a cusp feature starts to emerge around zero fields. Moreover, the MR shows no dependency on the bias current (**Supplementary Information**). The positive MR with a cusp has been attributed to WAL and the presence of a strong SOC, similar to that reported in thin metallic films and semiconductor heterostructures<sup>5,28,36,37</sup>. With the increase in  $d$ , the cusp feature becomes more prominent, which is an indication that the SOC becomes stronger in samples with a thicker LFO layer. A similar enhancement of the cusp feature has been observed in the LAO/STO heterostructure<sup>8,31</sup> under the application of large electric fields of up to 100 V. Even though LFO reduces the carrier density and shifts the Fermi level below universal Lifshitz transition, we still achieved fourfold SOC enhancement. Conventionally, in the electric-field induced SOC, the enhancement is always accompanied by the increase in the carrier density (Fermi level shift across energy bands, universal Lifshitz transition)<sup>26</sup>. On the contrary, our SOC enhancement is accompanied by a reduction in the carrier density in the absence of an external electric field.

To further understand the spin relaxation mechanism we determine the first-order quantum correction to the magnetoconductance,  $\Delta\sigma_S/\sigma_0 \equiv (\sigma_S(H)/\sigma_0 - 1)$ , by fitting it to the Maekawa-Fukuyama (MF) model<sup>38</sup>. The fitting model details are described in **Supplementary Information**. Our thickness-dependent magnetoconductance data can be fit well with this theory, considering two independent parameters inelastic ( $\tau_i$ ) and spin-orbit relaxation scattering time ( $\tau_{SO}$ ) evolving as a function of  $d$  (**Figure 3(a)**). This results in non-trivial evolution of effective inelastic ( $H_i$ ) and spin-orbit field ( $H_{SO}$ ), and elastic ( $\tau_e$ ), inelastic ( $\tau_i$ ), and spin-orbit relaxation scattering time ( $\tau_{SO}$ ) (**Figure 3(b)-(c)**). In particular, the effective spin-orbit field,  $H_{SO}$ , perceived by the electrons moving relativistically under the influence of the  $E_0$ , increases by an order of magnitude with  $d$ , while  $H_i$  remains nearly constant. Further, while  $\tau_i$  is almost constant at 2 ps for all samples, the  $\tau_{SO}$  decreases by one order of magnitude from 0.3 ps for the as-grown LAO-STO to 0.03 ps for the samples with a buffer layer. These results are consistent with the expectation from the MF model in the strong SOC regime where  $\tau_{SO} < \tau_i$ . We also find that the  $\tau_{SO}$  is inversely proportional to the  $\tau_e$  over the range of the  $d$  values in our experiment. This is a clear sign of the dominating DP spin relaxation mechanism<sup>39,40</sup> (via Rashba SOC) wherein the electron spins precess around the  $H_{SO}$  field with a corresponding Larmor frequency,  $\Omega(\mathbf{k})$  (see **Supplementary Information**). A similar spin relaxation mechanism was also reported in the gate tunable LAO/STO system<sup>8</sup>. We further determine the Rashba SOC coefficient  $\alpha_R$  from the relation  $\alpha_R = \hbar^2/(2m^*\sqrt{\tau_{SO}D})$ , where  $m^* = 3m_e$  is electron's effective mass<sup>41</sup>. Here, the Rashba effect lifts the double degeneracy of the  $3d$  orbitals and results in a spin splitting ( $\Delta_R = 2\alpha_R k_F$ ) of a few meV. **Figure 3(d)** demonstrates the enhancement of the SOC and the spin splitting due to the introduction of the carrier modulation layer. It is worth noting here that although the modulation layer and the electrostatic gating both can result in a SOC enhancement, the dependence of the  $\alpha_R$  and  $\tau_{SO}$  on the  $n_S$  is the opposite in the two cases. In the electrostatic gating, a positive back-gate voltage leads to an increase in the  $n_S$  as expected and thus results in the enhancement of the  $\alpha_R$  and  $\tau_{SO}$ . Whereas in our system, increasing the LFO thickness leads to a decrease in  $n_S$ , yet  $\alpha_R$  and  $\tau_{SO}$  increase significantly. We already explain this discrepancy using an asymmetric hopping of the orbital wave functions.

To compare the strength of the Rashba SOC of the heterostructures with and without the LFO layers, the Rashba coefficients at the  $\Gamma$  point of the lowest  $d_{xy}$  band were calculated (**Figure 3(e)**). Notably, the spin momentum locking is direct evidence of the presence of Rashba SOC in the STO band structure. The band structures of the LAO/LFO(4 uc)/STO and the LAO/STO including SOC are calculated along the  $\Gamma - M$  direction in the  $k$  space (see **Supplementary Information** for more detail). The interfacial symmetry breaking lifts the degeneracy of the Ti  $t_{2g}$  bands, resulting in the splitting between the  $d_{xy}$  and the  $d_{zx}, d_{yz}$  bands. The conduction band minimum is at the  $\Gamma$  point and is mainly contributed by the  $d_{xy}$  orbitals of the interface Ti-sites. For the standard Rashba SOC, the spin splitting  $\Delta$  is linearly dependent on  $k$ , where the Rashba coefficient  $\alpha_R$  can be defined as  $\Delta/2|k|^{42}$ . The Rashba coefficients of the heterostructures with and without LFO layers are 4.3 meV  $\text{\AA}$  and 0.6 meV  $\text{\AA}$ , respectively (**Figure 3(f)**). This result provides strong theoretical support to the experimentally observed enhancement of the Rashba coefficient due to the incorporation of the LFO layer.

To further understand the origin of the SOC tuning, we performed EELS in a cross-sectional STEM. The EELS data of LAO/LFO( $d$  uc)/STO are simultaneously acquired with ADF images where  $d = 0, 2,$  and  $4$  uc. Layer resolved Fe- $L$  and Ti- $L$  EELS at different  $\text{FeO}_2$  and  $\text{TiO}_2$  planes in LFO and STO layers are analysed and formation of  $\text{Fe}^{2+}$  and  $\text{Ti}^{3+}$  concentration and distribution for the  $d = 0, 2,$  and  $4$  uc samples are presented. A summary of the atomic layer resolved charge distribution for the  $d = 0, 2$  and  $4$  uc samples is depicted (see **Figure 4(a)-(c)**), where the reduced Ti and Fe fractions are defined as  $\Delta_{\text{Ti}} = \text{Ti}^{3+}/(\text{Ti}^{3+}+\text{Ti}^{4+})$  and  $\Delta_{\text{Fe}} = \text{Fe}^{2+}/(\text{Fe}^{2+}+\text{Fe}^{3+})$ , respectively. Clearly, the electron trapping in the LFO results in less free carriers in the STO layer compared to the control LAO/STO interface. From these results, we extract the integrated distribution ( $A_d$ ), width ( $w_d$ ) and peak ( $\Delta_{\text{Ti}}^1$ ) of the  $\text{Ti}^{3+}$  in the STO layers as a function of  $d$  (**Figure 4(d)-(f)**, respectively). Both  $\Delta_{\text{Ti}}^1$  and  $A_d$  decrease with  $d$ , suggesting that the  $\text{Ti}^{3+}$  decreases with the increase of the LFO thickness. This result agrees with our Hall data (**Figure 3(d)**), which show a suppression of total carrier density ( $n_S$ ), presumably in the Ti  $3d_{xy}$  conduction band. The  $w_d$ , which is related to the spatial width of the electronic

distribution, also decreases with  $d$ , suggesting that the spatial confinement of 2DES in STO increases in the presence of the LFO layers. These results provide insights into the role of LFO layers in tuning the inversion asymmetry and enhancing the effective electric field experienced by the 2DES<sup>43-45</sup>. This is one of the key ingredients underlying the strong enhancement of the Rashba spin-orbit coupling found in our magnetotransport experiments.

In conclusion, we provide fundamental role of lattice polarization mediated via antisymmetric orbital hybridization in establishing the observed enhancement of Rashba SOC. Our work opens a new way of introducing asymmetric orbital hopping and to utilize it for various applications, in particular as a consequence of the lattice polarization. First-principles calculations and ABF imaging have shown a clear evidence of polar distortions in the TiO<sub>2</sub> planes from the change in metal-oxygen-metal bond angles, hence contributing to the enhancement of SOC at STO interface. The strategies to tune and control the Rashba spin splitting at zero bias voltage is particularly promising as it can be integrated directly in functional devices for efficient spin-to-charge conversion<sup>46-49</sup>.

## References

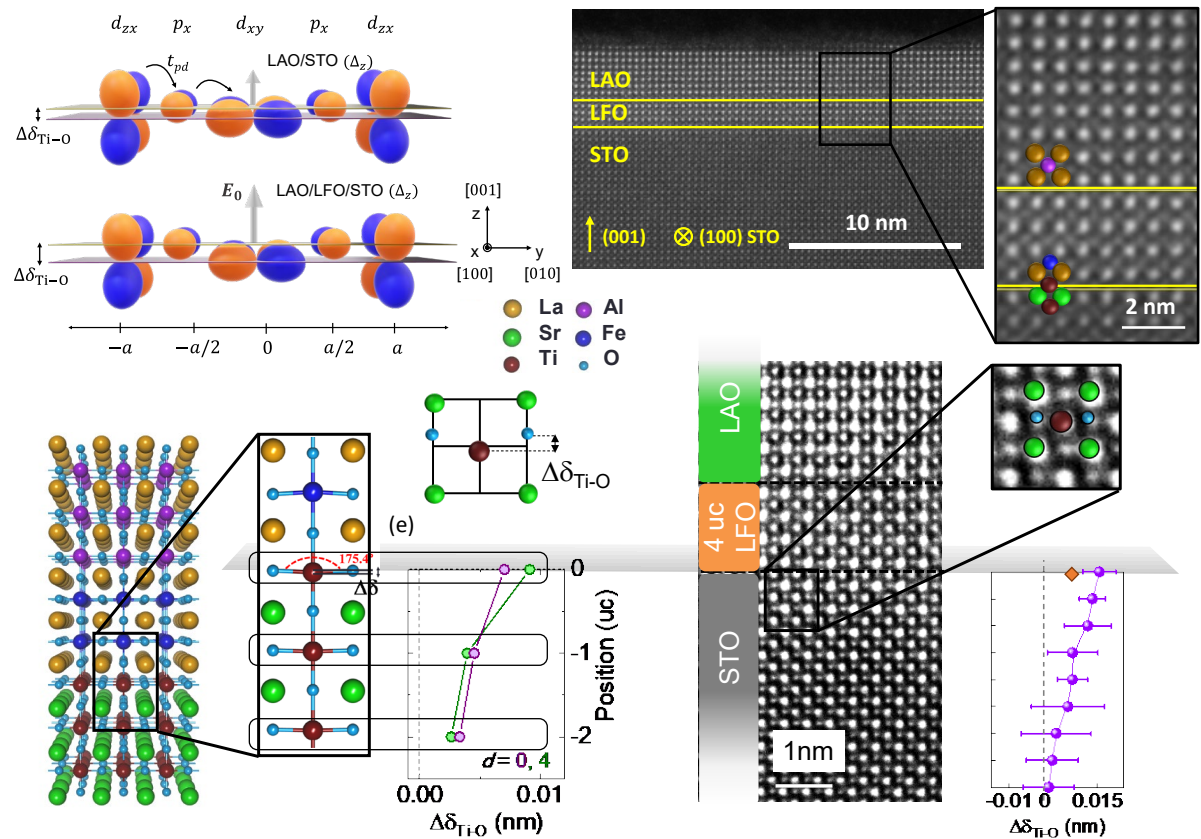
- 1 Rojas-Sánchez, J. C. *et al.* Spin to Charge Conversion at Room Temperature by Spin Pumping into a New Type of Topological Insulator:  $\alpha$ -Sn Films. *Phys. Rev. Lett.* **116**, 096602, (2016).
- 2 Deorani, P. *et al.* Observation of inverse spin Hall effect in bismuth selenide. *Phys. Rev. B* **90**, 094403, (2014).
- 3 Cheng, C., Sun, J.-T., Chen, X.-R., Fu, H.-X. & Meng, S. Nonlinear Rashba spin splitting in transition metal dichalcogenide monolayers. *Nanoscale* **8**, 17854-17860, (2016).
- 4 Sánchez, J. C. R. *et al.* Spin-to-charge conversion using Rashba coupling at the interface between non-magnetic materials. *Nat. Commun.* **4**, 2944, (2013).
- 5 Koga, T., Nitta, J., Akazaki, T. & Takayanagi, H. Rashba spin-orbit coupling probed by the weak antilocalization analysis in InAlAs/InGaAs/InAlAs quantum wells as a function of quantum well asymmetry. *Phys. Rev. Lett.* **89**, 046801 (2002).
- 6 Studer, M., Salis, G., Ensslin, K., Driscoll, D. C. & Gossard, A. C. Gate-Controlled Spin-Orbit Interaction in a Parabolic *GaAs/AlGaAs* Quantum Well. *Phys. Rev. Lett.* **103**, 027201, (2009).
- 7 Schultz, M. *et al.* Rashba spin splitting in a gated HgTe quantum well. *Semicond. Sci. Technol.* **11**, 1168-1172, (1996).
- 8 Caviglia, A. D. *et al.* Tunable Rashba spin-orbit interaction at oxide interfaces. *Phys. Rev. Lett.* **104**, 126803, (2010).
- 9 Žutić, I., Fabian, J. & Sarma, S. D. Spintronics: Fundamentals and applications. *Rev. Mod. Phys.* **76**, 323 (2004).
- 10 Wolf, S. *et al.* Spintronics: a spin-based electronics vision for the future. *Science* **294**, 1488-1495 (2001).
- 11 Winkler, R. Spin-orbit coupling effects in two-dimensional electron and hole systems. *Springer Tr. Mod. Phys.* **191**, 1-8 (2003).
- 12 Rashba, E. I. Properties of semiconductors with an extremum loop. I. Cyclotron and combinational resonance in a magnetic field perpendicular to the plane of the loop. *Sov. Phys., Solid State* **2**, 1109-1122 (1960).

- 13 Manchon, A., Koo, H. C., Nitta, J., Frolov, S. & Duine, R. New perspectives for Rashba spin-orbit coupling. *Nat. Mater.* **14**, 871-882 (2015).
- 14 Soumyanarayanan, A., Reyren, N., Fert, A. & Panagopoulos, C. Emergent phenomena induced by spin-orbit coupling at surfaces and interfaces. *Nature* **539**, 509-517 (2016).
- 15 Huang, Z. *et al.* Interface engineering and emergent phenomena in oxide heterostructures. *Adv. Mater.* **30**, 1802439 (2018).
- 16 Nakagawa, N., Hwang, H. Y. & Muller, D. A. Why some interfaces cannot be sharp. *Nat. Mater.* **5**, 204-209, (2006).
- 17 Ohtomo, A. & Hwang, H. A high-mobility electron gas at the LaAlO<sub>3</sub>/SrTiO<sub>3</sub> heterointerface. *Nature* **427**, 423 (2004).
- 18 Varignon, J., Vila, L., Barthélémy, A. & Bibes, M. A new spin for oxide interfaces. *Nat. Phys.* **14**, 322-325 (2018).
- 19 Khalsa, G., Lee, B. & MacDonald, A. H. Theory of 2 g electron-gas Rashba interactions. *Phys. Rev. B* **88**, 041302 (2013).
- 20 Kim, Y., Lutchyn, R. M. & Nayak, C. Origin and transport signatures of spin-orbit interactions in one-and two-dimensional SrTiO<sub>3</sub>-based heterostructures. *Phys. Rev. B* **87**, 245121 (2013).
- 21 Zhong, Z., Tóth, A. & Held, K. Theory of spin-orbit coupling at LaAlO<sub>3</sub>/SrTiO<sub>3</sub> interfaces and SrTiO<sub>3</sub> surfaces. *Phys. Rev. B* **87**, 161102 (2013).
- 22 Petersen, L. & Hedegård, P. A simple tight-binding model of spin-orbit splitting of *sp*-derived surface states. *Surf. Sci.* **459**, 49-56 (2000).
- 23 Gazquez, J. *et al.* Competition between polar and nonpolar lattice distortions in oxide quantum wells: New critical thickness at polar interfaces. *Phys. Rev. Lett.* **119**, 106102 (2017).
- 24 Omar, G. J. *et al.* Characteristic Lengths of Interlayer Charge-Transfer in Correlated Oxide Heterostructures. *Nano Lett.* (2020).
- 25 Reinle-Schmitt, M. L. *et al.* Tunable conductivity threshold at polar oxide interfaces. *Nat. Commun.* **3**, 932, (2012).
- 26 Joshua, A., Pecker, S., Ruhman, J., Altman, E. & Ilani, S. A universal critical density underlying the physics of electrons at the LaAlO<sub>3</sub>/SrTiO<sub>3</sub> interface. *Nat. Commun.* **3**, 1129 (2012).

- 27 Liang, H. *et al.* Nonmonotonically tunable Rashba spin-orbit coupling by multiple-band filling control in SrTiO<sub>3</sub>-based interfacial d-electron gases. *Phys. Rev. B* **92**, (2015).
- 28 Bergmann, G. Weak localization in thin films: a time-of-flight experiment with conduction electrons. *Phys. Rep.* **107**, 1-58 (1984).
- 29 Hikami, S., Larkin, A. I. & Nagaoka, Y. Spin-orbit interaction and magnetoresistance in the two dimensional random system. *Prog. Theor. Phys.* **63**, 707-710 (1980).
- 30 Stornaiuolo, D. *et al.* Tunable spin polarization and superconductivity in engineered oxide interfaces. *Nat. Mater.* **15**, 278 (2016).
- 31 Stornaiuolo, D. *et al.* Weak localization and spin-orbit interaction in side-gate field effect devices at the LaAlO<sub>3</sub>/SrTiO<sub>3</sub> interface. *Phys. Rev. B* **90**, 235426 (2014).
- 32 Shalom, M. B., Sachs, M., Rakhmilevitch, D., Palevski, A. & Dagan, Y. Tuning spin-orbit coupling and superconductivity at the SrTiO<sub>3</sub>/LaAlO<sub>3</sub> interface: a magnetotransport study. *Phys. Rev. Lett.* **104**, 126802 (2010).
- 33 Gopinadhan, K. *et al.* Gate Tunable In- and Out-of-Plane Spin-Orbit Coupling and Spin-Splitting Anisotropy at LaAlO<sub>3</sub>/SrTiO<sub>3</sub> (110) Interface. *Adv. Electron. Mater.* **1**, 00114, (2015).
- 34 Herranz, G. *et al.* Engineering two-dimensional superconductivity and Rashba spin-orbit coupling in LaAlO<sub>3</sub>/SrTiO<sub>3</sub> quantum wells by selective orbital occupancy. *Nat. Commun.* **6**, 6028, (2015).
- 35 Manipatruni, S. *et al.* Scalable energy-efficient magnetoelectric spin-orbit logic. *Nature* **565**, 35-42 (2019).
- 36 Iordanskii, S., Lyanda-Geller, Y. B. & Pikus, G. Weak localization in quantum wells with spin-orbit interaction. *ZhETF Pisma Redaktsiiu* **60**, 199 (1994).
- 37 Knap, W. *et al.* Weak antilocalization and spin precession in quantum wells. *Phys. Rev. B* **53**, 3912 (1996).
- 38 Maekawa, S. & Fukuyama, H. Magnetoresistance in two-dimensional disordered systems: effects of Zeeman splitting and spin-orbit scattering. *J. Phys. Soc. Jpn.* **50**, 2516-2524 (1981).
- 39 Dyakonov, M. & Perel, V. Spin relaxation of conduction electrons in noncentrosymmetric semiconductors. *Sov. Phys. Solid State, Ussr* **13**, 3023-3026 (1972).

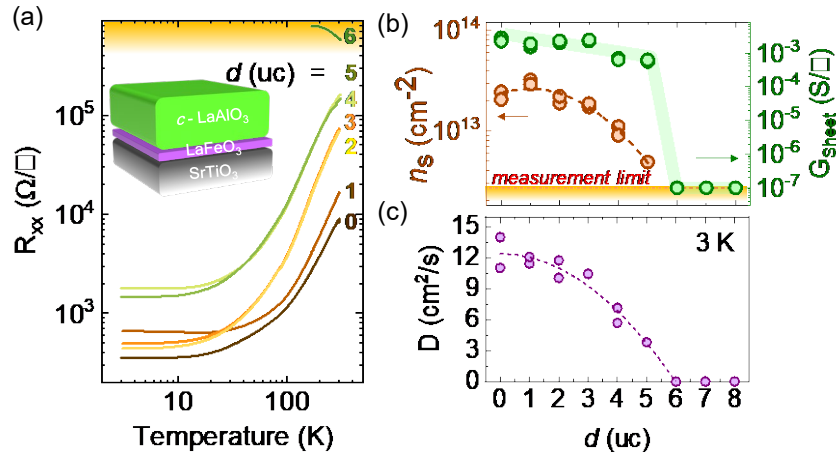
- 40 Szolnoki, L., Kiss, A., Dóra, B. & Simon, F. Spin-relaxation time in materials with broken inversion symmetry and large spin-orbit coupling. *Sci. Rep.* **7**, 1-10 (2017).
- 41 Mattheiss, L. Effect of the 110° K Phase Transition on the SrTiO<sub>3</sub> Conduction Bands. *Phys. Rev. B* **6**, 4740 (1972).
- 42 Shanavas, K., Popović, Z. S. & Satpathy, S. Theoretical model for Rashba spin-orbit interaction in *d* electrons. *Phys. Rev. B* **90**, 165108 (2014).
- 43 Liu, M. *et al.* Enhancement of Rashba spin-orbit coupling by electron confinement at the LaAlO<sub>3</sub>/SrTiO<sub>3</sub> interface. *J. Phys. Cond. Matter* **32**, 235003 (2020).
- 44 Herranz, G. *et al.* Engineering two-dimensional superconductivity and Rashba spin-orbit coupling in LaAlO<sub>3</sub>/SrTiO<sub>3</sub> quantum wells by selective orbital occupancy. *Nat. Commun.* **6**, 6028 (2015).
- 45 Kim, M., Ihm, J. & Chung, S. B. Strongly enhanced Rashba splittings in an oxide heterostructure: A tantalate monolayer on BaHfO<sub>3</sub>. *Phys. Rev. B* **94**, 115431 (2016).
- 46 Lesne, E. *et al.* Highly efficient and tunable spin-to-charge conversion through Rashba coupling at oxide interfaces. *Nat. Mater.* **15**, 1261 (2016).
- 47 Wang, Y. *et al.* Room-temperature giant charge-to-spin conversion at the SrTiO<sub>3</sub>-LaAlO<sub>3</sub> oxide interface. *Nano Lett.* **17**, 7659-7664 (2017).
- 48 Vaz, D. C. *et al.* Mapping spin-charge conversion to the band structure in a topological oxide two-dimensional electron gas. *Nat. Mater.* **18**, 1187-1193 (2019).
- 49 Noël, P. *et al.* Non-volatile electric control of spin-charge conversion in a SrTiO<sub>3</sub> Rashba system. *Nature* **580**, 483-486 (2020).

**Figure 1**



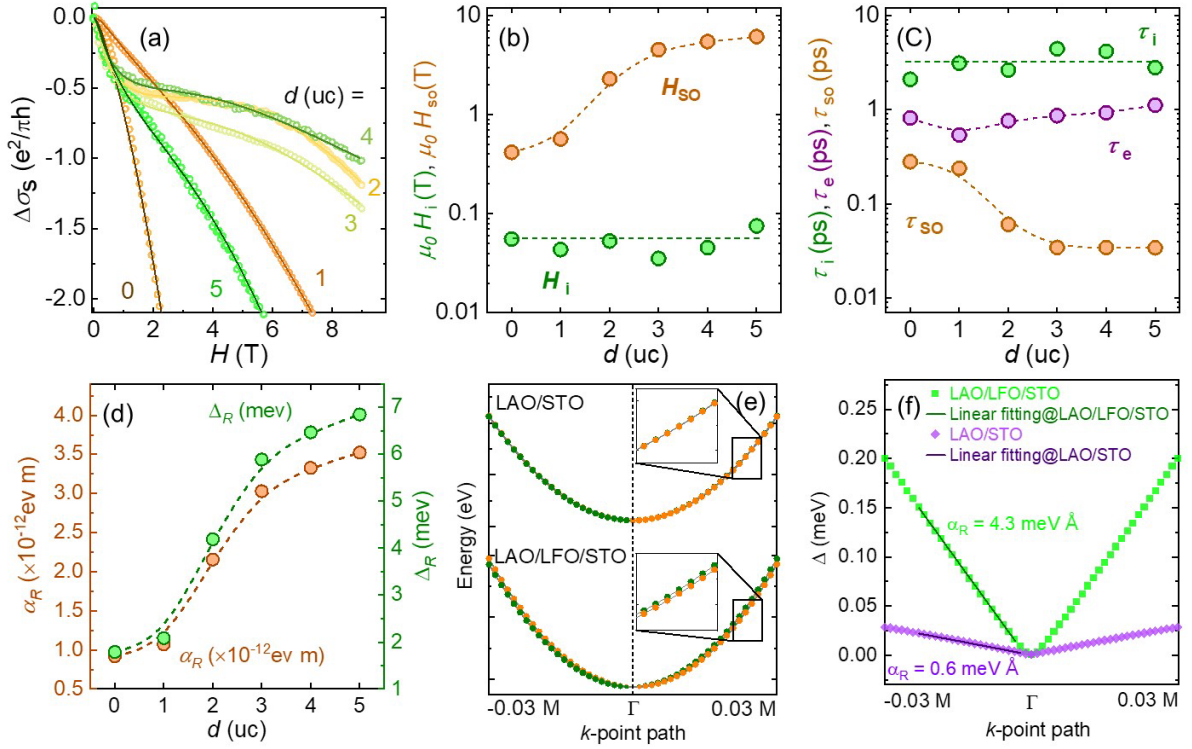
**Fig. 1 | Ionic displacement and asymmetric orbital hopping in metal-oxygen network.** (a) Orbital bonding network between Ti  $d_{zx}$  and  $d_{xy}$  asymmetric orbitals on neighbouring metal atoms through  $p_x$  orbitals along the  $y$  axis with built-in electric field ( $E_0$ ). Comparison of displacement of the Ti cation ( $d_{xy}, d_{zx}$  orbital) (top plane) and oxygen ( $p_x$ ) (bottom plane) sublattices in large built-in electric field for  $d = 0$  and 4 uc. The schematic positive and negative lobes of the orbital functions are represented in orange and blue, respectively. (b) ADF-STEM image of crystalline LAO/LFO(4 uc)/STO heterostructure. (c) Schematic figure of LAO/LFO(2 uc)/STO in the (001) crystallographic direction. (d) Ti-O-Ti ionic displacement ( $\Delta\delta_{\text{Ti-O}}$ ) along the [001] axis for the topmost  $\text{TiO}_2$  plane calculated from first-principles calculations. The schematics of ionic displacement patterns in the unit-cell structures (middle). (e),  $\Delta\delta_{\text{Ti-O}}$  of the  $\text{TiO}_2$  layer at a different depth from the interface for  $d = 0$  and 4 uc. (f) ABF-STEM results for LAO/LFO(4uc)/STO heterostructure. (g)  $\Delta\delta_{\text{Ti-O}}$  is calculated from the displacement (with error bar) along the [001] axis between the center position of Ti-site cation and the O-site anions using ABF mode in STEM.

Figure 2



**Fig. 2 | Modulation of the transport properties of 2DES interface.** (a) The temperature dependence of the transverse sheet resistance ( $R_{xx}$ ) for various  $d$  in 2DES heterostructure. With the characteristic length above  $d = 6 uc$  of LFO in heterostructure becomes insulating (yellow shaded area). (e), Left axis, orange circles: LFO-thickness-dependent carrier density ( $n_s$ ) and right axis, green circles: sheet conductance ( $G_{sheet}$ ) at 3 K. (f), Thickness dependent modulation of the diffusion coefficient  $D$  at 3 K. The dotted lines are guides to the eye.

**Figure 3**



**Fig. 3 | Spin-orbit coupling characteristics of 2DES interfaces.** (a) Conductance ( $\Delta\sigma_s$ ), normalized to  $e^2/\pi h$ , and best fits according to the Maekawa-Fukuyama theory for various  $d$  values. Experimental data are shown in open circles, whereas theoretical fits are shown in solid lines. (b),  $d$  dependence of the fitting parameters  $H_i$  (green circles) and  $H_{SO}$  (orange circles). (c), Inelastic relaxation time  $\tau_i$  (green circles), spin relaxation time  $\tau_{so}$  (orange circles) and elastic relaxation  $\tau_e$  (purple circles) as a function of  $d$  plotted on a logarithmic time scale. (d), Left axis, orange circles: Rashba SOC Coefficient,  $\alpha_R$  and right axis, green circles: Rashba spin splitting,  $\Delta_R$  as a function of  $d$ . The dotted lines are guides to the eye for all plots. (e) The closer zoomed-in DFT bands around the  $\Gamma$  point (zoom in Rashba spin splitting at a smaller range of  $k$ -point path, inset figures). The orange and dark green dots denote spin components with opposite directions (oriented along the  $y$  axis) lying perpendicular to the  $k$ -vector (along the  $x$  axis). The size of each dot denotes the magnitude of the corresponding spin component. (f), Rashba spin splitting for LAO/STO and LAO/LFO/STO shows the linear momentum dependence.

Figure 4

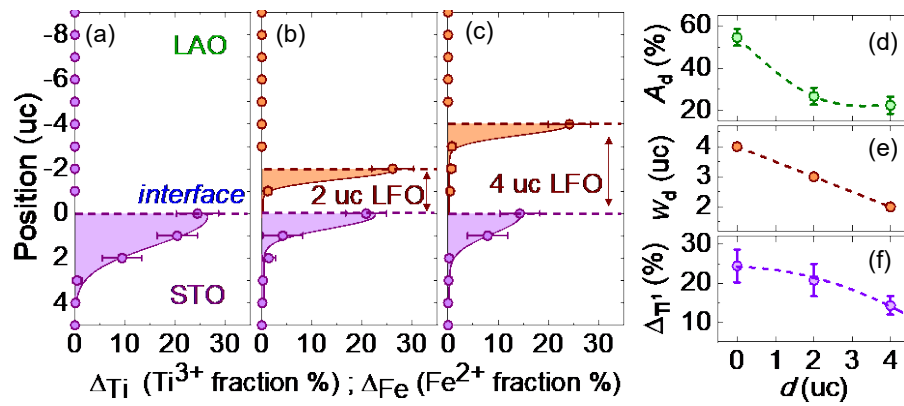


**Fig. 4 | Analysis of EELS spectroscopic data and electronic dimensionality.** (a)-(c), A summary of the atomic layer resolved charge distributions (with error bar) in % defined as the Ti<sup>3+</sup> fraction  $\Delta_{Ti} = Ti^{3+}/(Ti^{3+}+Ti^{4+})$  and Fe<sup>2+</sup> fraction  $\Delta_{Fe} = Fe^{2+}/(Fe^{2+}+Fe^{3+})$  for  $d =$  (a) 0, (b) 2, and (c) 4 uc. The lines are a guide to the eye. (g)-(i), The integrated distribution ( $A_d$ ), spatial width of the electronic distribution ( $w_d$ ) and peak ( $\Delta_{Ti}^1$ ) of the Ti<sup>3+</sup> species in the first interfacial layer of STO, as a function of  $d = 0, 2,$  and 4 uc. The dotted lines are a guide to the eye.

## **Acknowledgments**

This research is supported by the Agency for Science, Technology and Research (A\*STAR) under its Advanced Manufacturing and Engineering (AME) Individual Research Grant (IRG) (A2083c0054).

The authors also acknowledge the Singapore National Research Foundation (NRF) under the Competitive Research Programs (CRP Award No. NRF-CRP15-2015-01) for a partial support and the Centre for Advanced 2D Materials at National University of Singapore for providing computing resources.

## **Author Contribution**

G.J.O and A.A. designed and conceived the project. G. J. O. and W. K. contributed equally to this work. G.J.O. fabricated oxide high quality samples, performed low temperature magnetotransport experiments and fitting analysis. H.J. assisted for interpretation of the fitting analysis, theoretical model description and valuable suggestions. W.K. performed the first principles DFT calculations under the supervision of Z.J., L.S., Y.P.F. M.S.L. performed the TEM characterization and EELS analysis with their fitting. S.W. and L.Z.S. assisted for transport measurement and S.P and S.H assisted for film growth. G.J.O. and A.A. wrote the manuscript with help from other authors. All authors have given approval to the final version of the manuscript.

## **Competing interests**

The authors declare no competing interests.

## Methods

### Sample preparation and characterization.

500  $\mu\text{m}$ -thick  $\text{SrTiO}_3$  (STO) (001) substrates were treated with HF solution and annealed at temperature  $T = 950$  °C to obtain atomic steps and  $\text{TiO}_2$ -terminated surfaces. The STO substrates were patterned in a Hall bar and lateral gate electrode geometry by using conventional photolithography and amorphous highly insulating AlN films were deposited as a hard mask wall as shown in the inset of Figure S10. Pulsed laser deposition (PLD) method was used for sample preparation and the layer-by-layer growth was monitored by *in-situ* reflection high energy electron diffraction (RHEED). The  $\text{LaFeO}_3$  (LFO) layer thickness ( $d$  uc) was changed from 0 to 8 uc, while the  $\text{LaAlO}_3$  (LAO) layer thickness was kept fixed at 8 uc. A nanosecond KrF 248nm laser was used with fluence of  $1.5 \text{ Jcm}^{-2}$  and a repetition rate of 2 Hz to grow all samples. We used the growth parameters, with temperature  $T = 750$  °C, oxygen pressure  $P_{\text{O}_2} = 10$  mTorr to grow LFO layers and  $T = 740$  °C,  $P_{\text{O}_2} = 0.5$  mTorr to grow LAO layer on top.

### Transport Measurements.

The all-electrical transport measurements (sheet resistance, carrier density and mobility) were carried in a quantum design physical property measurement system (PPMS) with temperature range of 300 down to 3 K and magnetic fields up to 9 T. To determine the exact carrier density, a Hall bar pattern on STO substrate was designed by a standard photolithography process. All lithography processes were performed (including AlN hard mask deposition) before growing the samples to avoid any exposure to the chemicals which can deteriorate the quality of surface and interface. The wires are connected by Al ultrasonic wire bonding for transverse and longitudinal transport measurement.

### STEM Imaging and EELS Analysis.

TEM samples were prepared by a FIB (focused ion beam) system (FEI Versa 3D) with 30 kV Ga ions, followed by a low-voltage (i.e., 2 kV) cleaning step. STEM imaging was performed by a JEM-ARM200F (JEOL) microscope (operated at 200 kV), equipped with an ASCOR aberration corrector, a cold-field emission gun and a Gatan Quantum ER spectrometer. The EELS results were acquired using a collection angle of 100 mrad with the energy dispersion of 0.25 and 0.1 eV per channel for the

elemental mapping and energy loss near edge structure (ELNES), respectively. The EELS maps were subject to noise reduction by a principal component analysis (PCA) filter.

### **DFT Calculations.**

First-principles calculations were performed using density-functional theory (DFT) based Vienna *ab initio* simulation package (VASP). Perdew-Burke-Ernzerhof (PBE) approximation was used in the calculations to describe the electron exchange-correlations<sup>44-46</sup>. Interactions between electrons and ions were described using the projector augmented wave (PAW) potentials<sup>47</sup>. PBE+ Hubbard  $U$  of 2.5 eV and 8 eV were applied to Fe  $d$  orbitals and the unoccupied La  $f$  orbitals, respectively, to include the on-site Coulomb interactions<sup>48</sup>. The electronic wave functions were expanded using the plane-wave basis set with a cut-off energy of 500 eV. A  $\sqrt{2} \times \sqrt{2} \times 1$  supercell of the vacuum/LAO/LFO/STO slab model was used to simulate the G-type antiferromagnetism of LFO layers in the LAO/LFO/STO heterostructure. For comparison,  $\sqrt{2} \times \sqrt{2} \times 1$  supercell of the vacuum/LAO/STO slab model was used to simulate the LAO/STO heterostructure. The thicknesses of LAO, LFO, and STO were set to 6, 4, and 4 uc, respectively, and the vacuum layers were set to about 20 Å to minimize electronic interactions between periodic images.  $\Gamma$ -centered  $k$ -point grids for sampling the first Brillouin zone were set to  $8 \times 8 \times 1$  for the  $\sqrt{2} \times \sqrt{2} \times 1$  supercells of both vacuum/LAO/STO and vacuum/LAO/LFO/STO slabs. All atoms except those of the bottom STO layer were relaxed until the force on each atom is less than 0.02 eV/Å.

## Method References

- 50 Kresse, G. & Hafner, J. Ab initio molecular dynamics for liquid metals. *Phys. Rev. B* **47**, 558 (1993).
- 51 Kresse, G. & Hafner, J. Ab initio molecular dynamics for open-shell transition metals. *Phys. Rev. B* **48**, 13115 (1993).
- 52 Kresse, G. & Furthmüller, J. Efficiency of ab-initio total energy calculations for metals and semiconductors using a plane-wave basis set. *Comput. Mater. Sci.* **6**, 15-50 (1996).
- 53 Kresse, G. & Joubert, D. From ultrasoft pseudopotentials to the projector augmented-wave method. *Phys. Rev. B* **59**, 1758 (1999).
- 54 Dudarev, S., Botton, G., Savrasov, S., Humphreys, C. & Sutton, A. Electron-energy-loss spectra and the structural stability of nickel oxide: An LSDA+ U study. *Phys. Rev. B* **57**, 1505 (1998).

## *Supplementary Information*

### **Large Rashba Spin-Orbit Effect by Orbital Engineering at SrTiO<sub>3</sub>-based Correlated Interfaces**

G. J. Omar<sup>1,†</sup>, W. L. Kong<sup>1,†</sup>, H. Jani<sup>1</sup>, M. S. Li<sup>2</sup>, J. Zhou<sup>1</sup>, Z. S. Lim<sup>1</sup>, S. Prakash<sup>1</sup>, S. W. Zeng<sup>1</sup>, S. Hooda<sup>3</sup>, T. Venkatesan<sup>3</sup>, Y. P. Feng<sup>1</sup>, S. J. Pennycook<sup>2</sup>, L. Shen<sup>4</sup>, A. Ariando<sup>1,\*</sup>

#### **Affiliations:**

<sup>1</sup>Department of Physics, Faculty of Science, National University of Singapore, Singapore 117542, Singapore

<sup>2</sup>Department of Materials Science and Engineering, National University of Singapore, Singapore 117575, Singapore

<sup>3</sup>Department of Electrical and Computer Engineering, National University of Singapore, Singapore 117576, Singapore

<sup>4</sup>Department of Mechanical Engineering, National University of Singapore, Singapore, 117575

\*Correspondence should be sent to [ariando@nus.edu.sg](mailto:ariando@nus.edu.sg)

<sup>†</sup>[Authors contributed equally.](#)

## **Content**

**S1. Theory of  $t_{2g}$  electron-gas Rashba interactions.**

**S2. The fit of the magnetoconductance curves using the theoretical models.**

**S3. First-principles calculations of the heterostructures.**

**S4. STEM and EELS analysis**

**S5. Structural characteristics of 2DES interface.**

**S6. Transport characteristics of 2DES interface.**

## S1. Theory of $t_{2g}$ electron-gas Rashba interactions.

Two-dimensional electron gas where the confined electrons of the conduction band are in Ti-3d orbitals, splits into  $t_{2g}(3d_{xy}, 3d_{xz,yz})$  and  $e_g(3d_{x^2-y^2}, 3d_{z^2})$  orbitals due to crystal field. The interfacial symmetry breaking lifts the degeneracy of the Ti  $t_{2g}$  bands, resulting in the splitting between the  $d_{xy}$  and the  $d_{zx}, d_{yz}$  bands. The Hamiltonian for these  $t_{2g}$  bands of Ti cations at the top layer of STO is defined as  $H = H_0 + H_{ASO} + H_z$  where  $H_0 = H_{\text{atomic}} + \Delta U$ ,  $H_{\text{atomic}}$  defined as atomic orbital Hamiltonian and  $\Delta U$  is the terms related to the hopping terms between nearest-neighbor orbital.  $H_{ASO} + H_z$  are the perturbed hopping Hamiltonian terms. Here,  $H_{ASO}$  is on-site atomic SOC and  $H_z$  is antisymmetric inter-orbital hopping. In the simplistic electronic structure,  $t_{2g}$   $xy$  orbitals on one B site can hop only along the  $y$  or  $x$  direction through an intermediate  $p_x$  or  $p_y$  orbital to an  $xy$  orbital on the B site of a neighbouring cubic cell<sup>1</sup>.

$$H_0 = \begin{pmatrix} \frac{k_x^2}{2m_h} + \frac{k_y^2}{2m_l} & 0 & 0 \\ 0 & \frac{k_x^2}{2m_h} + \frac{k_y^2}{2m_l} & 0 \\ 0 & 0 & \frac{k_x^2}{2m_h} + \frac{k_y^2}{2m_l} - \Delta_E \end{pmatrix} \otimes \sigma^0 \begin{Bmatrix} yz \\ zx \\ xy \end{Bmatrix}, \quad (S1)$$

where,  $\Delta_E$  is the energy difference between the  $d_{xy}$  band and the  $d_{xz}, d_{yz}$  orbitals due to the transverse confinement along the  $z$  direction.  $H_{ASO}$  is atomic spin-orbit coupling projected to  $t_{2g}$  orbital bands,

$$H_{ASO} = \Delta_{ASO} \begin{pmatrix} 0 & i\sigma_z & -i\sigma_y \\ -i\sigma_z & 0 & i\sigma_x \\ i\sigma_y & -i\sigma_x & 0 \end{pmatrix} \begin{Bmatrix} yz \\ zx \\ xy \end{Bmatrix}, \quad (S2a)$$

$$= \begin{pmatrix} 0 & 0 & i & 0 & 0 & -1 \\ 0 & 0 & 0 & -i & 1 & 0 \\ -i & 0 & 0 & 0 & 0 & i \\ 0 & i & 0 & 0 & i & 0 \\ 0 & 1 & 0 & -i & 0 & 0 \\ -1 & 0 & -i & 0 & 0 & 0 \end{pmatrix} \begin{Bmatrix} yz, \uparrow \\ yz, \downarrow \\ zx, \uparrow \\ zx, \downarrow \\ xy, \uparrow \\ xy, \downarrow \end{Bmatrix}, \quad (S2b)$$

where,  $\Delta_{ASO}$  is atomic spin-orbit mixing term.  $H_z$  is antisymmetric interorbital nearest-neighbour hopping, a layer dependent term, induced by polar lattice displacement due to the electric field ( $E_0$ ) from broken inversion symmetry.

$$H_z = \Delta_z \begin{pmatrix} 0 & 0 & ik_x \\ 0 & 0 & ik_y \\ -ik_x & -ik_y & 0 \end{pmatrix} \otimes \sigma^0 \begin{Bmatrix} yz \\ zx \\ xy \end{Bmatrix}, \quad (S3)$$

where,  $\Delta_z$  generates hopping terms from  $d_{xy}$  to  $d_{xz}$  only in the  $y$  direction through  $p_x$  and from  $d_{xy}$  to  $d_{yz}$  only in the  $x$  direction through  $p_y$ . The perturbation arises from additional potential  $-eE_0z$ , which induce hopping amplitude as  $E_0\gamma_1$ , where  $\gamma_1 = \left\langle d_{zx}, \vec{R} = 0 | -ez | p_x, \vec{R} = \frac{a}{2}\hat{y} \right\rangle$

In the second-order perturbation,  $\text{Ti}(3d_{xy}) - \text{O}(2p_x) - \text{Ti}(3d_{xy})$  hopping described by the effective transfer integral  $t_{1,2}$  as below,

$$t_{1,2} = \frac{\left\langle d_{xy}, \vec{R} = 0 | H_0 | p_x, \vec{R} = \frac{a}{2}\hat{y} \right\rangle \left\langle p_x, \vec{R} = \frac{a}{2}\hat{y} | H_0 | d_{xy}, \vec{R} = a\hat{y} \right\rangle}{\Delta_{pd}} \quad (S4)$$

$$t_{1,2} = \frac{t_{pd}^2}{\Delta_{pd}} \quad (S5)$$

where,  $t_{pd}$  is the orbital hopping amplitude of the  $p - d$  hybridization and  $\Delta_{pd}$  is the splitting between the oxygen  $p$  and Ti  $t_{2g} 3d_{xy}$  orbital. In the second order perturbation,  $\text{Ti}(3d_{zx}) - \text{O}(2p_x) - \text{Ti}(3d_{xy})$  hopping is defined as (Figure S1),

$$\Delta_z = \frac{\left\langle d_{zx}, \vec{R} = 0 | -eE_0z | p_x, \vec{R} = \frac{a}{2}\hat{y} \right\rangle \left\langle p_x, \vec{R} = \frac{a}{2}\hat{y} | H_0 | d_{xy}, \vec{R} = a\hat{y} \right\rangle}{\Delta_{pd}} \quad (S6)$$

$$\Delta_z = \frac{E_0\gamma_1 t_{pd}}{\Delta_{pd}} \quad (S7)$$

Finally, the expectation value of second-order perturbed Hamiltonian,

$$\begin{aligned} & \langle k, d_{xy}\sigma' | H^{(2)} | k, d_{xy}, \sigma \rangle \\ &= \sum_{k', \sigma''} \frac{\langle k, d_{xy}\sigma' | H_z | k', d_{xz}, \sigma'' \rangle \langle k', d_{xz}\sigma'' | H_{ASO} | k, d_{xy}, \sigma \rangle}{E_{d_{xz}}(k') - E_{d_{xy}}(k)} \\ & \quad + \frac{\langle k, d_{xy}\sigma' | H_z | k', d_{yz}, \sigma'' \rangle \langle k', d_{yz}\sigma'' | H_{ASO} | k, d_{xy}, \sigma \rangle}{E_{d_{yz}}(k') - E_{d_{xy}}(k)} \\ &= \epsilon_{xy}(\vec{k}) - \frac{\Delta_z \Delta_{ASO}}{\Delta_E} [\langle \sigma_y \rangle k_x a - \langle \sigma_x \rangle k_y a] \end{aligned} \quad (S8)$$

$$= \epsilon_{xy}(\vec{k}) - \alpha_R (\vec{k} \times \vec{\sigma}) \cdot \hat{z}$$

where,  $\alpha_R \sim \frac{\Delta_z \Delta_{ASO}}{\Delta_E} a$ , defined as conventional Rashba spin-orbit coupling, valid for small  $k$  and for the  $xy$  band. Notably, the Rashba parameter is directly proportional to the asymmetric hopping term  $\Delta_z$ , which is directly related to the induced orbital polarization and the atomic displacement.

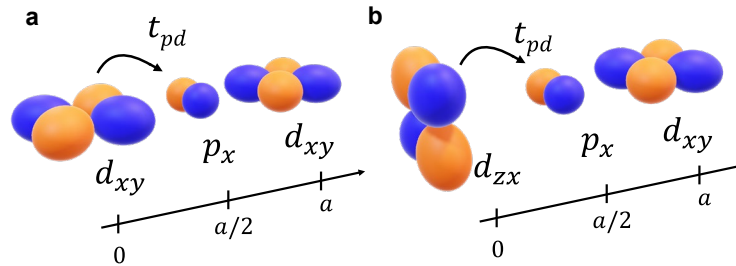


**Figure S1** Schematic figure of the Ti metal and oxygen orbitals at the STO interface resulting in a,  $\text{Ti}(3d_{xy}) - \text{O}(2p_x) - \text{Ti}(3d_{xy})$  and b,  $\text{Ti}(3d_{zx}) - \text{O}(2p_x) - \text{Ti}(3d_{xy})$  hopping with the hopping amplitude  $t_{pd}$ .

## S2. The fit of the magnetoconductance curves using the theoretical models.

The Iordanskii, Lyanda-Geller, and Pikus (ILP)<sup>2</sup> is the most developed and widely used theoretical model reported in the literature for the comprehensive description of WL/WAL phenomena. This theory considers both the  $k$ -linear and  $k$ -cubic components of Rashba interactions, where  $k$  is the wave vector of the electronic carriers. Here, the quantum correction of the magnetoconductance due to the SOC is given as,

$$\begin{aligned} \frac{\Delta\sigma_S(H)}{\sigma_0} = & -\frac{1}{a_0} - \frac{2a_0 + 1 + H_{SO}/H}{a_1 \left( a_0 + H_{SO}/H \right) - 2 H'_{SO}/H} \\ & + \sum_{n=1}^{\infty} \left[ \frac{3}{n} - \frac{3a_n^2 + 2a_n H_{SO}/H - 1 - 2(2n+1) H'_{SO}/H}{\left( a_n + H_{SO}/H \right) a_{n-1} a_{n+1} - 2 H'_{SO}/H [(2n+1)a_n - 1]} \right] \\ & - 2 \ln \frac{H_{tr}}{H} - \psi \left( \frac{1}{2} + \frac{H_i}{H} \right) - 3c \end{aligned} \quad (S9)$$

where  $a_n = n + \frac{1}{2} + \frac{H_i}{H} + \frac{H_{SO}}{H}$ ,  $H_i = \frac{\hbar}{4eD\tau_i}$ ,  $H_{tr} = \frac{\hbar}{4eD\tau_1}$ ,  $H_{SO} = \frac{\hbar}{4eD} (2\Omega_1^2\tau_1 + 2\Omega_3^2\tau_3)$ ,  $H'_{SO} = \frac{\hbar}{4eD} 2\Omega_1^2\tau_1$ ,  $\frac{1}{\tau_m} = \int (1 - \cos m\theta) W(\theta) d\theta$ ,  $\psi(1+z) = -c + \sum_{n=1}^{\infty} \frac{z}{n(n+z)}$ ,  $\psi$  is the digamma function,  $c$  is the Euler constant,  $H_{tr}$  is the elastic scattering field of electrons.  $\tau_1$  is the elastic scattering time which can be calculated from the carrier concentration  $n_S$  and mobility  $\mu_S$ .  $m = 1$  or  $3$  and  $W(\theta)$  the probability of scattering by a scattering angle  $\theta$ .  $\sigma_0 = e^2/\pi\hbar$  is a universal value of quantum conductance.

As we mentioned, Equation S9 includes both the  $k$ -linear  $\overline{\Omega}_1$  and  $k$ -cubic  $\overline{\Omega}_3$  spin-orbit terms, where vector  $\overline{\Omega}$  is the precession of spins and its direction defines the axis of the precession. It is also related to the spin-splitting parameter  $\Delta_R$  through the relation,  $\Delta_R = \hbar|\overline{\Omega}|$ . The ILP theory includes both field-dependent and -independent terms, where independent- or zero-field contribution also needs to be subtracted according to the experiments. Moreover, omitting the  $H'_{SO}$  contribution from the Equation S9 can easily lead to the well-known Hikami-Larkin-Nagoaka (HLN) theory<sup>3</sup>, where only the  $k$ -cubic spin-orbit is present. Later, Maekawa-Fukuyama (MF) model<sup>4</sup> was developed with the inclusion of the Zeeman effect. This model is based on the contribution of the D'yakonov-Perel spin precession

mechanism<sup>5</sup>, and therefore, it is used to describe the Rashba Coefficients at our oxide interfaces. Generally, the Zeeman effect is suppressed due to the strong SOC with the perpendicular magnetic field.

$$\begin{aligned} \frac{\Delta\sigma_S(H)}{\sigma_0} = & \psi\left(\frac{H}{H_i + H_{so}}\right) + \frac{1}{2\sqrt{1-\gamma^2}} \psi\left(\frac{H}{H_i + H_{so}(1 + \sqrt{1-\gamma^2})}\right) \\ & - \frac{1}{2\sqrt{1-\gamma^2}} \psi\left(\frac{H}{H_i + H_{so}(1 - \sqrt{1-\gamma^2})}\right) \end{aligned} \quad (S10)$$

Additionally, the contribution from the classical orbital term is added to the Equation S10,

$$\Delta\sigma_{orb} = A_k \frac{H_0}{\sigma_0} \left( \frac{H^2}{1 + cH^2} \right) \quad (S11)$$

which becomes relevant at high magnetic fields. In order to estimate the classical orbital term, we first used Equation S11 to fit the high field region (between 4 and 9 T) of our data and obtained an estimation of the parameter  $A_k$ . Then, we performed a complete fit of the magnetoconductance curve, using the MF formula in Equation S10, with the addition of the S11 term. This process yielded good fits and parameters with high accuracy, for all values of  $d$ .

### S3. First-principles calculations of the heterostructures.

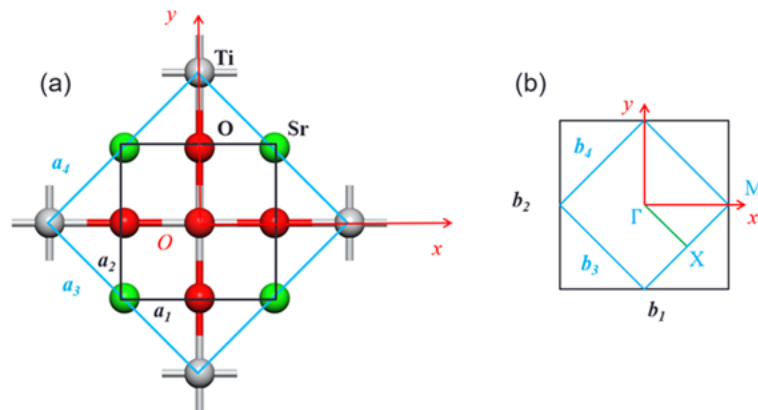


**Figure S2.** (a) Schematic top views of the unit cell (defined by solid black lines) and  $\sqrt{2} \times \sqrt{2} \times 1$  supercell (defined by solid blue lines) of the LAO/LFO/STO (LAO/STO) heterostructure, where  $a_1$  and  $a_2$  denote in-plane lattice parameters of the unit cell while  $a_3$  and  $a_4$  denote in-plane lattice parameters of the supercell. (b) Schematic top views of first Brillouin zones of the unit cell (defined by solid black lines) and  $\sqrt{2} \times \sqrt{2} \times 1$  supercell (defined by solid blue lines) of the LAO/LFO/STO (LAO/STO) heterostructure, where  $b_1$ ,  $b_2$ ,  $b_3$ , and  $b_4$  denote reciprocal lattice parameters corresponding to  $a_1$ ,  $a_2$ ,  $a_3$ , and  $a_4$  in (a), respectively. The  $x$ -direction of the supercell in (a) is along the Ti-O bond while it is along  $\Gamma - M$  of the reciprocal lattice of the supercell in (b).

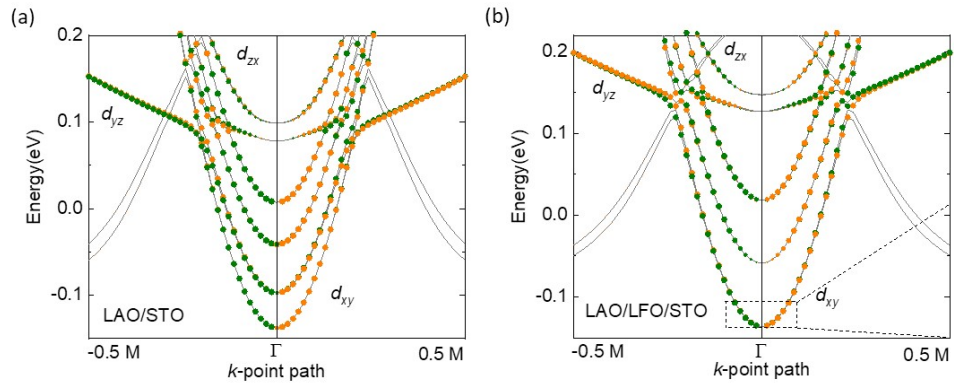


**Figure S3.** Band structure of  $t_{2g}$   $d$ -orbitals in the STO layer of the LAO/STO and LAO/LFO/STO interface. The orange and dark green dots denote spin components with opposite directions (oriented along the  $y$  axis) lying perpendicular to the  $k$ -vector (in the  $\Gamma - M$ ) (along the  $x$  axis). The size of each dot denotes the magnitude of the corresponding spin component. Oxygen  $p$  bands are in grey colour.

#### S4. STEM and EELS analysis

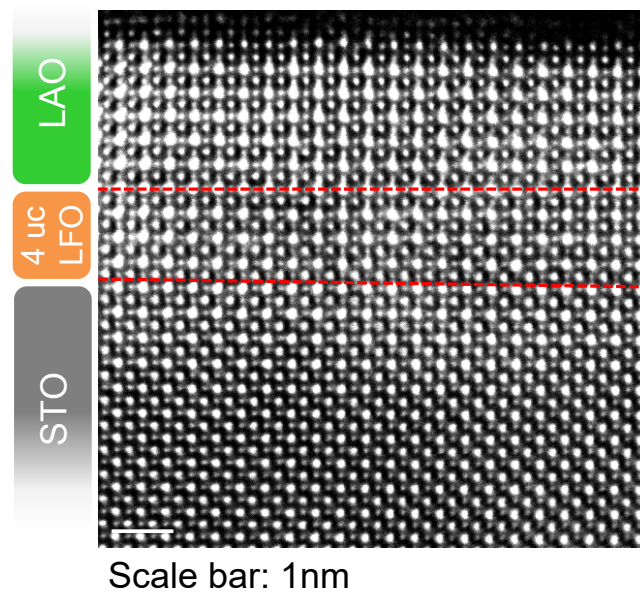


**Figure S4.** Annular bright-field scanning transmission electron microscopy (ABF-STEM). ABF-STEM results for LAO/LFO(4uc)/STO heterostructure. The ABF is more sensitive to the tilt of the electron beam with respect to the crystal zone axis than the ADF, and therefore oxygen atom columns can clearly be resolved.

The STEM images for LAO/LFO/STO heterostructures with  $d = 0, 2,$  and  $4$  uc also consistently present a coherent and epitaxial growth with sharp interfaces shown in **Figure S5, S6, S7, and S8**. As discussed earlier, the charge transfer associated with the formation of  $\text{Ti}^{3+}$ -ions at the top layer of the STO results in a 2DES at the LAO/STO interface. In the presence of a LFO buffer layer, a fraction of the transferred electrons would be trapped in the LFO layer leading to the formation of  $\text{Fe}^{2+}$ -ions at the LAO/LFO interface. Analysing the EELS of the  $\text{Fe-}L_{2,3}$  edges of the  $d = 2$  uc sample confirms that 26.2% (1.2%) of the Fe atoms in the top (bottom) LFO layer indeed changes from  $\text{Fe}^{3+}$  to  $\text{Fe}^{2+}$  (Figure S5(b)). Likewise, as shown in Figure S5(c), the  $\text{Ti-}L_{2,3} e_g$  peaks confirm that 20.8% and 4.2% of Ti atoms at the topmost and second unit-cell layers of the STO change the valency from  $4+$  to  $3+$ , while it remains  $4+$  for the rest of the STO layer underneath. The  $\text{Fe}^{2+}$  and  $\text{Ti}^{3+}$  concentration and distribution for the  $d = 0, 2$  and  $4$  uc samples are presented in Figure S6, S7 and S8.

To extract the changes in the valency of cationic species, we analysed the energy shifts in the Ti- $L_{2,3}$  and Fe- $L_{2,3}$  edges. The Ti- $L_{2,3}$   $e_g$  peaks extracted from the interfacial layers shift toward lower binding energy, indicating a decreasing Ti valence from 4+ to 3+. Hence, the energy difference between  $L_3$   $e_g$ - $t_{2g}$  edges is used to calculate the  $\text{Ti}^{3+}$  fraction relative to overall Ti species but is not apparent in the Fe- $L_{2,3}$  edges. So, a Voigt function fitting is performed to calculate the intensity ratio between  $L_3$  and  $L_2$ , which validates the Fe valence change from  $\text{Fe}^{3+}$  to  $\text{Fe}^{2+}$ . This indicates the presence of larger  $\text{Fe}^{2+}$  and  $\text{Ti}^{3+}$  fractions near to the LAO/LFO and the LFO/STO interfaces, respectively.

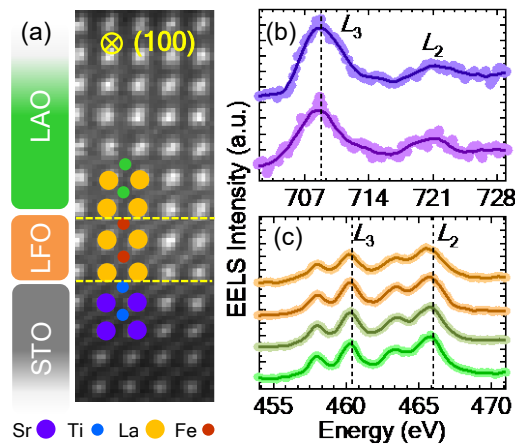


**Figure S5.** (a) An ADF image of LAO/LFO(2uc)/STO simultaneously acquired with EELS data. (b)-(c) Layer resolved Fe- $L$  and Ti- $L$  EELS at different  $\text{FeO}_2$  and  $\text{TiO}_2$  planes in the 2-uc-thick LFO and 4-uc-STO layers, respectively. The light-coloured dots are original data, and the dark-coloured solid lines are smoothed data by Fast Fourier Transform (FFT). The intensity ratio  $L_3/L_2$  is used to extract  $\text{Fe}^{2+}$  fraction and  $L_3$   $e_g$ - $t_{2g}$  is used to calculate  $\text{Ti}^{3+}$  fraction.

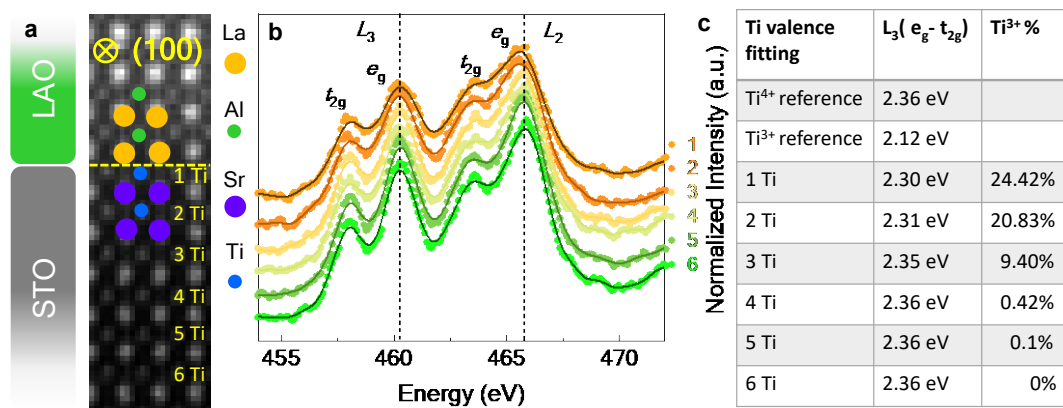


**Figure S6.** a, An ADF image of LAO/STO heterostructure simultaneously acquired with EELS data. b, Layer resolved EELS at different TiO<sub>2</sub> planes (numbered 1 through 6) in the STO substrate. A combination of the Gaussian and Lorentzian functions was used to fit the Ti-  $L_{2,3}$  edge peaks and the results are summarized in the table. c, the sum of Ti<sup>3+</sup> fractions in the top 3-4 planes adds up about ~50% and reduces to 0% for the rest of the TiO<sub>2</sub> planes.

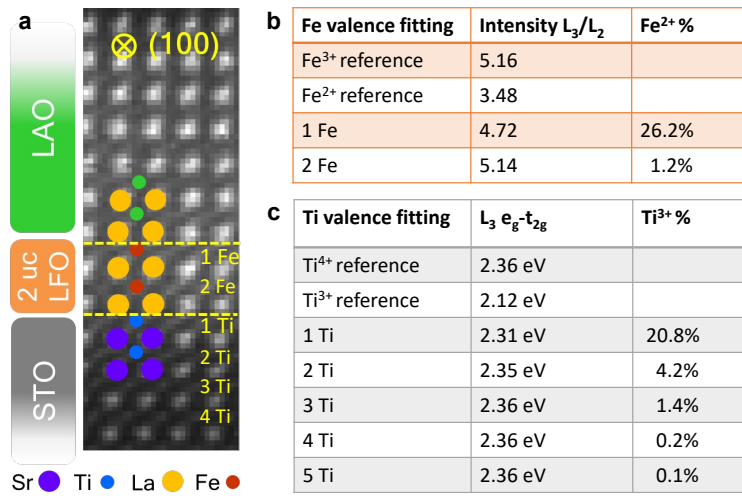


**Figure S7.** a, An ADF image of LAO/LFO(2 uc)/STO heterostructure simultaneously acquired with EELS data. A combination of Gaussian and Lorentzian functions was used to fit the Fe and Ti-  $L_{2,3}$  edge peaks. The results are summarized in tables (b) and (c). b, Fe<sup>2+</sup> fraction is 26±5% in the top FeO<sub>2</sub> plane near the LAO/LFO interface (1 Fe) and reduces to nearly 0% for 2 Fe. c, the sum of Ti<sup>3+</sup> fractions in the top 2 planes are about ~25% and reduces to 0% for the rest of the TiO<sub>2</sub> planes.

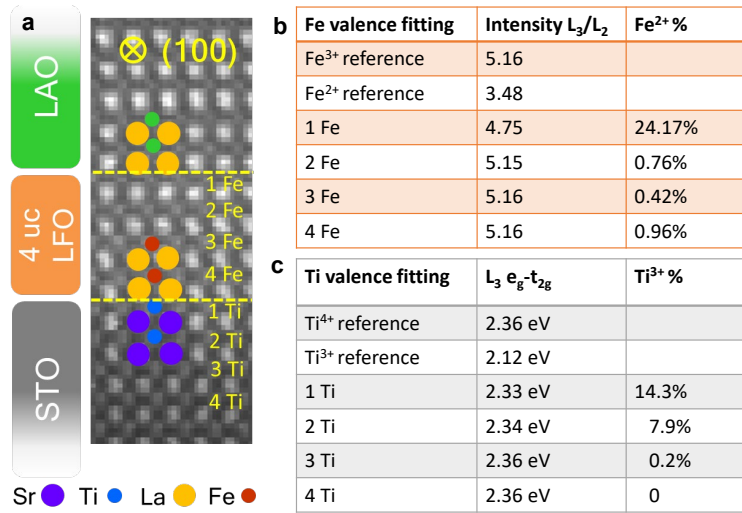


**Figure S8.** a, An ADF image of LAO/LFO(4 uc)/STO heterostructure simultaneously acquired with EELS data. A combination of Gaussian and Lorentzian functions was used to fit the Fe and Ti-  $L_{2,3}$  edge peaks. The results are summarized in tables (b) and (c). b, Fe<sup>2+</sup> fraction is 24±5% in the top FeO<sub>2</sub> plane near the LAO/LFO interface (1 Fe) and reduces to 0 for the rest of the FeO<sub>2</sub> planes. c, the sum of Ti<sup>3+</sup> fractions in the top 2 planes are about ~25% and reduces to 0% for the rest of the TiO<sub>2</sub> planes.

## S5. Structural characteristics of 2DES interface.

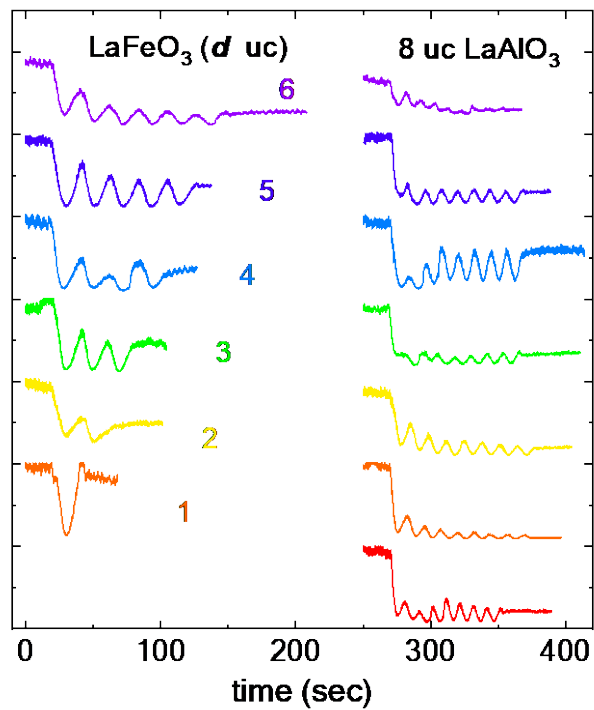


**Figure S9.** Layer-by-layer growth of LaFeO<sub>3</sub> with variable thickness ( $d = 0$  to 6 uc) and 8 uc LaAlO<sub>3</sub> on TiO<sub>2</sub> terminated SrTiO<sub>3</sub> interfaces determined by *in-situ* RHEED oscillations. We monitored the electrons reflection peak intensity along the (001) crystallographic direction during each growth, clearly signifies high-quality samples.

### S6. Transport characterization of 2DES interface.

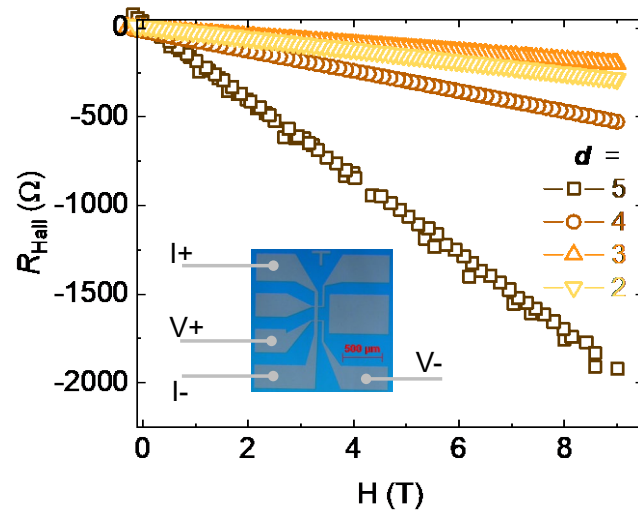


**Figure S10.** Hall resistance ( $R_{\text{Hall}}$ ) versus magnetic field  $H$  for different thickness ( $d$ ) of LFO, A linear Hall effect is observed for all different thickness of LFO buffer layers. Inset is a Hall bar pattern on STO substrate was designed by a standard photolithography process.

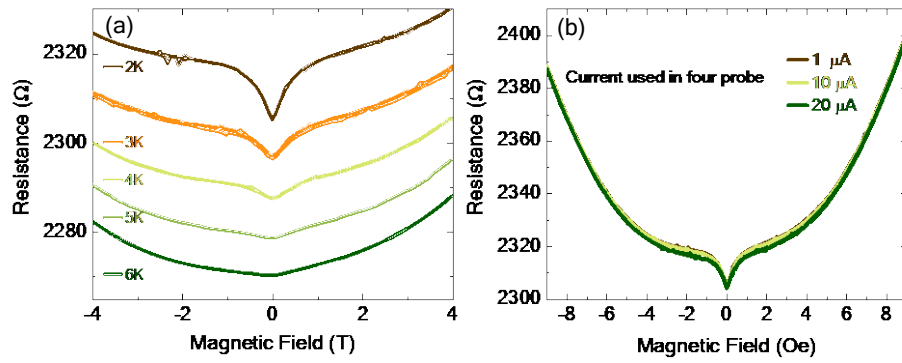


**Figure S11.** Temperature and current dependence on anomalous magnetoresistance. (a) The magnetoresistance curves measured for 2  $\mu\text{c}$  LFO spacer on LAO/STO structure as a function for temperature, between 2 K to 6 K. The minimum of the curve is determined mainly by the value of  $H_{\text{SO}}$ . From the plot, the minimum shifts with temperature, reflecting the decrease in the spin-orbit scattering field. (b) Magnetoresistance curves measured at different applied current values of 1, 10 and 20  $\mu\text{A}$ .

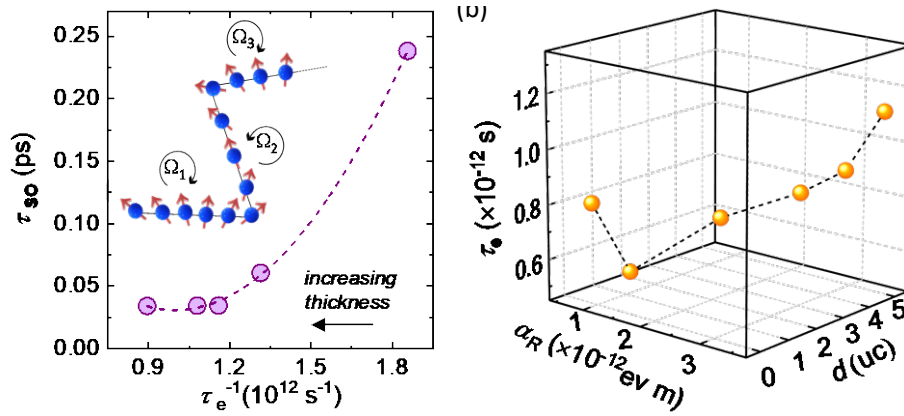


**Figure S12.** Magnetotransport characteristics of the 2DES interface. (a) Spin relaxation time ( $\tau_{so}$ ) vs elastic scattering rate ( $\tau_e$ ) dependency is consistent with D'yakonov-Perel' spin-relaxation mechanism (the electron spin precesses around the SOC fields and scatter on a timescale with a different vector of the SOC field corresponding Larmor frequency  $\Omega_i$ , inset figure). (b) scattering time (long carrier lifetime,  $\tau_e$ ) and Rashba coefficients  $\alpha_R$  plotted 3D as a function of the  $d$ .

## References

1. L. Mattheiss, *Physical Review B* **6**, 4718 (1972).
2. S. Iordanskii, Y. B. Lyanda-Geller, and G. Pikus, *ZhETF Pisma Redaktsiiu* **60**, 199 (1994).
3. S. Hikami, A. I. Larkin, and Y. Nagaoka, *Progress of Theoretical Physics* **63**, 707 (1980).
4. S. Maekawa and H. Fukuyama, *Journal of the Physical Society of Japan* **50**, 2516 (1981).
5. M. Dyakonov and V. Perel, *Soviet Physics Solid State, Ussr* **13**, 3023 (1972).